



1 **Development of a three-dimensional variational assimilation**
2 **system for lidar profile data based on a size-resolved aerosol**
3 **model in WRF-Chem model v3.9.1 and its application in PM_{2.5}**
4 **forecasts across China**

5
6 Yanfei Liang^{1,2}, Zengliang Zang¹, Dong Liu³, Peng Yan⁴, Yiwen Hu⁵, Yan Zhou⁶, Wei You¹

7
8 ¹Institute of Meteorology and Oceanography, National University of Defense Technology,
9 Nanjing, China.

10 ²No.32145 Unit of PLA, Xinxiang, China

11 ³Key Laboratory of Atmospheric Optics, Institute of Optics & Fine Mechanics, Chinese
12 Academy of Sciences, Hefei, China

13 ⁴Meteorological Observation Center, Chinese Meteorological Administration, Beijing,
14 China

15 ⁵Nanjing University of Information Science & Technology, Nanjing, China

16 ⁶No.78127 Unit of PLA, Beijing, China

17

18

19

20

21

22

23

24 *Corresponding author: Wei You (ywlx_1987@163.com); Zengliang
25 (zzlqxy@163.com)

26

27



28 **Abstract:**

29 For the aerosol variables in the model for simulating aerosol interactions
30 and chemistry (MOSAIC)-4bin chemical scheme in the Weather Research and
31 Forecasting–Chemistry (WRF–Chem) model, this study presents an
32 observation forward aerosol extinction coefficient (AEC) and aerosol mass
33 concentration (AMC) operator and corresponding adjoint based on the
34 interagency monitoring of protected visual environments (IMPROVE)
35 equation, and then a three-dimensional variational (3-DVAR) data assimilation
36 system (DA) is developed for lidar AECs and AMCs. DA experiments are
37 conducted based on AEC profiles measured by five light detection and ranging
38 (lidar) systems as well as mass concentration (MC) data measured at over
39 1,500 ground environmental monitoring stations across China for particulate
40 matter 2.5 μm or less in diameter ($\text{PM}_{2.5}$) and PM between 2.5 and 10 μm in
41 diameter (PM_{10}). An experiment comparing assimilated and without
42 assimilated measurements finds the following. While only five lidars were
43 available within the simulation region (approximately 2.33 million km^2 in
44 size), assimilating lidar AEC data alone can effectively improve the accuracy
45 of the initial field of the WRF–Chem as well as its forecast performance for
46 $\text{PM}_{2.5}$ MCs. Compared to the without assimilated experiment, DA reduces the
47 root mean square error of surface $\text{PM}_{2.5}$ MCs in the initial field of the model by
48 10.5 $\mu\text{g}/\text{m}^3$ (17.6%). Moreover, the positive effect resulting from the
49 optimization of the initial field for AMCs can last for more than 24 h. By
50 taking advantage of lidar aerosol vertical profile information and the
51 near-surface PM MC observations, assimilating lidar AEC and surface $\text{PM}_{2.5}$
52 (PM_{10}) simultaneously can effectively integrate their observed information and
53 generate a more accurate 3D aerosol analysis field.

54
55
56



57 **1. Introduction**

58 Aerosol data assimilation (DA) generates a three-dimensional (3D)
59 gridded analysis field capable of describing the spatial distribution of aerosols
60 by integrating numerical forecasts produced by an air quality model (AQM)
61 and measured aerosol data. With integrated information from various sources,
62 this analysis field can more accurately describe the 3D distribution pattern of
63 aerosols (Carmichael et al., 2008; Benedetti et al., 2009; Sandu et al., 2011;
64 Bannister, 2017). On the one hand, the analysis field generated by DA can be
65 used to effectively study atmospheric aerosol transmission patterns by
66 analyzing products of a certain time series and, on this basis, further examine
67 the effects of aerosols on human health, the environment, the weather, and the
68 climate (Baraskar et al., 2016). On the other hand, the analysis field can be
69 used as the initial chemical conditions for an AQM. The forecast performance
70 of the AQM for aerosols can then be enhanced by improving the accuracy of
71 the initial chemical conditions (Wu et al., 2015).

72 Compared to meteorological and marine DA, aerosol DA techniques are
73 still undeveloped. There is also a lack of variety when it comes to assimilable
74 measured data, which mainly include conventional surface aerosol mass
75 concentration (AMC) data and satellite-derived aerosol optical depth (AOD)
76 data. Of these two types of data, surface AMC data directly provide mass
77 concentration (MC) information for near-surface aerosols. The AOD is a
78 measure of the total extinction effects of aerosols in the vertical atmospheric
79 column. Thus, AOD data indirectly provide atmospheric-column
80 concentration information of aerosols. Assimilating either of these two types
81 of data can significantly improve the accuracy of the aerosol analysis field
82 (Tombette et al., 2008; Niu et al., 2008; Schwartz et al., 2012; Jiang et al.,
83 2013; Li et al., 2013; Saide et al., 2013; Yumimoto et al., 2015, 2016; Tang et
84 al., 2017; Peng et al., 2017; Xia et al., 2019; Wang et al., 2020), but these two
85 types of data are unable to provide vertical aerosol profiles. Consequently,



86 while these two types of data are abundant, have relatively high horizontal
87 resolutions, and cover a wide range of space, they play a very limited role in
88 optimizing the vertical structure of aerosols in the analysis field. To further
89 improve the accuracy of the vertical structure of aerosols, it is necessary to
90 assimilate measurements that contain vertical aerosol profile information.
91 Zang et al. (2016) assimilated aircraft-measured vertical concentration profiles
92 of aerosol components and found that while the profile data were limited in
93 quantity and covered a relatively small area, they could still significantly
94 improve the forecast accuracy of the AQM. Since direct observations of
95 concentration profiles require great amounts of labor and financial resources,
96 relatively few studies involving the acquisition and assimilation of this type of
97 data have been reported.

98 Light detection and ranging (lidar) can be used to capture
99 aerosol-backscattered laser signals at various heights. By inverting these
100 signals, the aerosol extinction coefficient (AEC) and aerosol backscattering
101 coefficient (ABC) can be determined, which indirectly provide vertical AMC
102 profile information (Fernald et al., 1984; Sugimoto et al., 2008, Raut et al.,
103 2009). Assimilating lidar aerosol data can help to improve the accuracy of the
104 vertical structure of aerosols in the analysis field (Sugimoto et al., 2009;
105 Tesche et al., 2007; Dilip et al., 2009; Young, S. A., and M. A. Vaughan, 2009;
106 Burton et al., 2010; Lolli et al., 2014; Chen et al., 2015). In addition, with the
107 increasing number of lidar stations and the development of lidar network
108 detection technology, there is great theoretical and application value to
109 studying lidar DA in order to generate more accurate 3D aerosol analysis
110 fields.

111 Compared to the assimilation of direct AMC measurements, the
112 assimilation of lidar AEC data faces myriad difficulties, of which establishing
113 an observation operator for the DA cost function is the most challenging. AEC
114 is the object of DA (i.e., observation variable), whereas the AMCs of various

115 types of aerosol variables in the AQM are to be optimized. To directly
116 determine optimal model aerosol variables by solving the DA cost function, it
117 is necessary to map the aerosol variables in the AQM to the observation space
118 by conducting a forward process on the observation operator (Kahnert et al.,
119 2008), corresponding to the calculation of the AMC from the AEC. In addition,
120 in 3D variational DA, it is also necessary to conduct the reverse process on the
121 observation operator when calculating the gradient of the cost function (Sandu
122 et al., 2011). The computational program for this adjoint process on the
123 observation operator relies on its forward process. The computational load and
124 the size of the program code increase nonlinearly with the complexity of the
125 forward process. Moreover, when it comes to aerosol variables, there are
126 many kinds of chemicals and particle-size bins. As a result, the chemical
127 model inherently involves a high computational load. Therefore, when using a
128 variational method to assimilate lidar data, it is necessary to take into
129 consideration both the accuracy and complexity of the observation operator.
130 Currently, there are three main methods that could be used to design
131 observation operators. (1) Directly using the Mie equation. Under the
132 assumption that aerosol particles are uniform and spherical, the Mie equation
133 can describe the scattering and extinction properties of aerosol particles of any
134 scale and with any chemical and physical parameters (Cheng et al., 2019).
135 However, since accurately solving the Mie equation involves a nonlinear
136 calculation process that contains iterations, it is extremely complicated to
137 implement, upgrade, and maintain the program for the reverse process on the
138 observation operator. In addition, due to the lack of reliable measurements of
139 essential aerosol parameters (e.g., complex refractive index, particle number
140 spectrum, and hygroscopicity), in practice it is necessary to introduce
141 assumptions about these parameters in DA schemes. This renders it difficult to
142 realize the high-accuracy advantage of DA schemes in practice. (2) Using the
143 community radiative transfer model (CRTM). This model is advantageous

144 because it gives the Jacobian term needed for the reverse process on the
145 observation operator when conducting its forward process, so that introducing
146 the CRTM to a DA scheme does not require separate numerical computational
147 programming for the reverse process on the observation operator (Liu and
148 Weng, 2006). DA schemes based on the CRTM have been applied in AOD
149 DA research and yielded excellent results (Liu et al., 2011). However, the
150 CRTM was developed for the Goddard Chemistry Aerosol Radiation and
151 Transport (GOCART) aerosol scheme in the Weather Research and
152 Forecasting–Chemistry (WRF–Chem) model. As a result, when applying the
153 CRTM to other AQMs and aerosol schemes, it is necessary to design
154 corresponding variable transformation interfaces (Cheng et al., 2019), which
155 will introduce additional errors. (3) Using the interagency monitoring of
156 protected visual environments (IMPROVE) equation. The IMPROVE
157 equation maps a relation between AMC and AEC (Lowenthal et al., 2003;
158 Ryan et al., 2005; Pitchford et al., 2007; Gordon et al., 2018). With relatively
159 high computational accuracy, this method has been used to evaluate model
160 performance and the extinction contributions of various aerosols (Kim et al.,
161 2006; Roy et al., 2007; Tao et al., 2009, 2012, 2014; Cao et al., 2012a, 2012b).
162 In addition, as its highest-order term is quadratic, the IMPROVE equation has
163 low nonlinearity. Therefore, using the IMPROVE equation to design an
164 observation operator can significantly reduce the complexity of the DA
165 program. To date, no operator design based on the IMPROVE equation and
166 subsequent variational lidar DA have been reported.

167 Some progress has been made in lidar DA. For example, Sekiyama et al.
168 (2010) used the Kalman filter DA method to assimilate ABC and AEC
169 profiles acquired by the Cloud-Aerosol Lidar and Infrared Pathfinder Satellite
170 Observations mission and applied the assimilated data to a global chemical
171 transport model. Wang et al. (2013, 2014a, and 2014b) studied the
172 assimilation of range-corrected lidar signals using the optimal interpolation

173 DA method and conducted an assimilation experiment based on data captured
174 by 12 lidar positioned in the Mediterranean Basin and one lidar positioned on
175 the French island of Corsica. They found that the improvement brought by DA
176 to the forecast performance for $PM_{2.5}$ lasted for approximately 36 hours.
177 However, in the above-mentioned studies, sequential DA methods were used,
178 and there is no particular need to take into consideration the complexity of the
179 observation operator. Cheng et al. (2019) assimilated lidar AEC profiles using
180 a 3D variational DA method with an observation operator based on the CRTM,
181 which was designed for the relatively simple GOCART dust aerosol scheme.

182 This study presents an observation operator and corresponding adjoint
183 module developed for the AEC based on the IMPROVE equation. This
184 observation operator module is introduced into the DA system developed by
185 Li et al. (2013) and Zang et al. (2016) for the model for simulating aerosol
186 interactions and chemistry (MOSAIC) aerosol scheme oriented to the
187 WRF–Chem model. DA and forecast experiments are conducted based on data
188 captured by five lidars (located in Beijing, Shijiazhuang, Taiyuan, Xuzhou,
189 and Wuhu, respectively) as well as data collected at approximately 1,500
190 ground environmental monitoring stations for $PM_{2.5}$ and PM_{10} .

191 **2. Materials and Methods**

192 **2.1. AQM**

193 The WRF–Chem model version 3.9.1 was selected as the AQM. The
194 model has 40 vertical layers between the surface and 50 hPa, with the
195 resolution gradually decrease from the bottom up. The model domains are
196 double-nested, and the second domain (D02) is centered at (114.57°E,
197 37.98°N) and has 175×166 grid points with a grid interval of 9 km. D02
198 covers the central and eastern regions of China (most of North China, northern
199 Central China, northern East China, and eastern Northwest China) (Figure 1).

200 The MOSAIC_4bin aerosol scheme was adopted for simulations. This scheme
201 can describe eight aerosol types. For each aerosol type, there are four
202 particle-size bins (4bin). The following summarizes other physical and
203 chemical schemes used in this study: the carbon-bond mechanism version Z
204 (CBMZ) chemical reaction mechanism, the fast-J photolysis calculation
205 scheme, the rapid radiative transfer model for general circulation models
206 (RRTMG) shortwave radiation scheme, the RRTMG longwave radiation
207 scheme, the WRF single-moment 5-class microphysical scheme, the unified
208 Noah land-surface parameterization scheme, the Grell 3D ensemble cumulus
209 parameterization scheme, the Yonsei University planetary boundary layer
210 scheme, and the revised MM5 Monin–Obukhov near-surface layer scheme.

211

212 **2.2. Data**

213 AEC profiles used in this study were derived from data captured by five
214 lidars (positioned in Beijing, Shijiazhuang, Taiyuan, Xuzhou, and Wuhu,
215 respectively) between 0000 and 1200 Coordinated Universal Time (UTC) on
216 November 13, 2018 (Figure 1) at a wavelength of 532 nm. The temporal
217 resolution of the data measured by the lidars in Shijiazhuang, Taiyuan,
218 Xuzhou, and Wuhu is 1 min, i.e., data were captured and a vertical AEC
219 profile was derived every minute. The vertical resolution of these data is 7.5 m,
220 i.e., one AEC was determined in one profile 7.5m away from the next one.
221 The blind spot of these lidars is 100 m, i.e., these systems cannot effectively
222 capture AEC data between the height of 100 m and the surface. The temporal
223 and vertical resolution of the AEC profiles captured by the lidar in Beijing are
224 1 h and 15 m, respectively, and the blind spot of this lidar system is 210 m. To
225 improve the effects of DA, it is necessary to first perform quality control on
226 and preprocess the original AEC profiles. This will ensure that the data are of
227 relatively high temporal and spatial representativeness and that the Lidar data
228 match the numerical model in terms of temporal and spatial resolution.



229 Quality control mainly involves four steps. (1) Entire AEC profiles passing
230 through low clouds and AEC measurements in mid- and high-cloud regions
231 are eliminated. An AEC profile is deemed to pass through low clouds when
232 the AEC in the near-surface layer (below 150 m) is lower than $3,000 \times 10^{-6} \text{ m}^{-1}$
233 and there is an AEC higher than $5,000 \times 10^{-6} \text{ m}^{-1}$ below 800 m. AEC
234 measurements in mid- and high-cloud regions are determined as follows: If the
235 AEC in the near-surface layer (below 150 m) is lower than $3,000 \times 10^{-6} \text{ m}^{-1}$,
236 then measurements higher than $5,000 \times 10^{-6} \text{ m}^{-1}$ on the AEC profile are of
237 AECs in mid- and high-cloud regions. (2) AEC profile data are subjected to
238 maximum and minimum control. AEC measurements higher than $3,000 \times 10^{-6}$
239 m^{-1} are each reassigned with a value of $3,000 \times 10^{-6} \text{ m}^{-1}$. AEC measurements
240 lower than $20 \times 10^{-6} \text{ m}^{-1}$ are eliminated. (3) Spatial continuity verification.
241 Valid data should be continuous within a certain continuous vertical space L_{con}
242 which is set to be 90 m in this study. Specifically, two metrics are used to
243 examine the spatial continuity of data. First, the profile with vertical resolution
244 L_{res} is examined. After the first two steps of quality control, the remaining
245 number of data points (N_{remain}) within the L_{con} should not be less than 1/3 the
246 total number of data points within the L_{con} ($N_{\text{total}} = L_{\text{con}}/L_{\text{res}}$); otherwise, it is
247 considered that no valid data are available for the center of the L_{con} . Second,
248 the deviation of the valid data from the mean value of the data within the L_{con}
249 does not exceed 3times the standard deviation (SD). (4) Blind detection spot
250 verification. Data within the blind spot of a lidar are eliminated. In addition,
251 considering that lidar signals are relatively weak and AMCs are very low
252 above 5,000 m, data for the region above 5,000 m are also eliminated in this
253 study.

254 Preprocessing of quality control-treated AEC profiles involves two steps.
255 (1) Temporal and spatial smoothing. Profiles are subjected to moving
256 averaging over 30 m in the vertical direction. Temporally, AEC profiles are
257 also averaged over the past hour. (2) Data thinning. Only one valid data point

258 is selected for assimilation between two adjacent model layers in the vertical
259 direction. In this study, the nearest data below each model layer are selected
260 for assimilation. After processing, the number of assimilated AEC
261 measurements on each profile does not exceed 25.

262 $PM_{2.5}$ and PM_{10} data (hereinafter referred to as PM data) used in this
263 study, including 1-h MC data collected at more than 1,500 ground
264 environmental monitoring stations, originated from the China National
265 Environmental Monitoring Center. Most of the monitoring stations are
266 distributed in cities in economically developed regions, including the Yangtze
267 River Delta, the Beijing–Tianjin–Hebei region, and the Pearl River Delta. Of
268 these monitoring stations, more than 790 are located within the D02 region
269 (Figure 1). DA experiments are performed in this study based on PM data
270 collected between 00:00 and 12:00 UTC on November 13, 2018. Subsequently,
271 forecasts for $PM_{2.5}$ from 12:00 UTC on November 13, 2018 to 12:00 UTC on
272 November 14, 2018 are produced. In addition, the effects of DA on the
273 forecast performance of the model are evaluated based on surface $PM_{2.5}$
274 measurements. To improve the effects of DA and the representativeness of the
275 evaluation metrics, the original PM data are subjected to quality-control and
276 preprocessing treatments. Quality control mainly involves two steps. (1)
277 Anomaly elimination. Measurements that remain unchanged over a continuous
278 period of 24 h are considered anomalous records and removed. (2) Maximum
279 and minimum control. $PM_{2.5}MC$ measurements higher than $600 \mu\text{g}/\text{m}^3$,
280 $PM_{10}MC$ measurements higher than $1,200 \mu\text{g}/\text{m}^3$, and PM MC measurements
281 less than 0 are considered anomalies and removed. During the DA and
282 verification processes, there may be multiple PM MC measurements for one
283 grid cell. To allow the measurements to represent the average PM MC within
284 a certain area, the PM data used for DA and verification are subjected to
285 grid-cell averaging. The PM data used for assimilation are averaged within
286 5×5 grid cells. Specifically, the PM data within the same 5×5 grid cell area are



287 first examined to determine their spatial consistency. Data greater than twice
288 the SD are removed. Then, the arithmetic mean of the data within the area is
289 calculated and assimilated. The PM_{2.5}MC measurements used for verification
290 and model forecasts are averaged within 1×1 grid cells. Specifically, model
291 forecasts are first interpolated to the location of each ground environmental
292 monitoring station. Then, the arithmetic mean of the measured and forecasted
293 values within the same grid cell is calculated and used as a sample for
294 quantifying the evaluation metrics. The processed PM MC data for the D01
295 and D02 regions are all assimilated. Only the PM_{2.5}MC data for the D02
296 region are used to evaluate the effects of DA. After the grid-cell averaging
297 treatment, approximately 190 data points in the D02 region are assimilated
298 each time.

299 **2.3. Basic theoretical DA model**

300 To mathematically achieve 3D variational DA, it is necessary to establish
301 an objective function to transform the DA problem to a problem of finding the
302 extreme value of the function. By calculating the extreme value of the function
303 using the variational method, an “optimal” analysis field will be obtained. The
304 following shows the mathematical form of such a function:

$$J(x) = \frac{1}{2}(x - x^b)^T B^{-1}(x - x^b) + \frac{1}{2}(Hx - y)^T R^{-1}(Hx - y) \quad (1)$$

305 This function describes the sum of the distance between the analysis field
306 (x) and the background field (x^b) and the distance between the analysis field (x)
307 and the observation field (y), with the background error covariance B and the
308 observation error covariance R as weights, respectively. In Equation (1), x is
309 the control variable in the DA system, which is a one-dimensional (1D) vector
310 composed of aerosol variables at all the 3D grid cells in the DA analysis field;
311 x^b is the background value (or best guess) of the control variable (as the
312 forecast level of AQM increases, model forecasts are generally used as

313 background fields); B is the background error covariance; y is the observation
314 variable, which is a 1D vector composed of all the measurements; H is the
315 observation operator, which maps the control variable to the observation space
316 to ensure that the observation data can provide observation information for the
317 control variable even if they are not direct measurements of the control
318 variable; and R is the observation error covariance. For simultaneous
319 assimilation of two or more types of observation data, the second term on the
320 right side of Equation (1) can be expanded to multiple terms, each of which
321 corresponds to one type of observation data. This will facilitate the
322 simultaneous assimilation of observation data from various sources.

323 **2.4. Control variables and B**

324 The MOSAIC_4bins aerosol scheme adopted in this study can describe
325 eight aerosol types, namely, black/elemental carbon (EC/BC), organic carbon
326 (OC), sulfates (SO_4^{2-}), nitrates (NO_3^-), ammonium salts (NH_4^+), chlorides
327 (Cl^-), sodium salts (Na^+), and other unclassified inorganic compounds (OIN).
328 There are four particle-size bins (4bin) for each aerosol type, namely,
329 0.039–0.1, 0.1–1.0, 1.0–2.5, and 2.5–10 μm . Thus, there are a total of 32
330 model variables that describe aerosols. Due to limitations of computer
331 memory and computational capacity, there cannot be an excessively large
332 number of control variables. In addition, fine ($\text{PM}_{2.5}$) and coarse ($\text{PM}_{2.5-10}$)
333 particles differ relatively significantly in AEC. Thus, two control variables,
334 namely, the sum of the first three particle-size bins (corresponding to fine
335 particles) and the fourth particle-size bin (corresponding to coarse particles),
336 are designed for each aerosol type, so that there are 16 control variables are
337 designed in this study for the DA scheme namely $\text{EC}_{2.5}$, $\text{EC}_{2.5-10}$, $\text{OC}_{2.5}$,
338 $\text{OC}_{2.5-10}$, $\text{SO}_4_{2.5}$, $\text{SO}_4_{2.5-10}$, $\text{NO}_3_{2.5}$, $\text{NO}_3_{2.5-10}$, $\text{NH}_4_{2.5}$, $\text{NH}_4_{2.5-10}$, $\text{CL}_{2.5}$, $\text{CL}_{2.5-10}$,
339 $\text{NA}_{2.5}$, $\text{NA}_{2.5-10}$, $\text{OIN}_{2.5}$, $\text{OIN}_{2.5-10}$.

340 Calculation associated with B is burdened with two problems: (1) An

341 overly large scale of B . In this scheme, B contains 3.5×10^{14} (= 16 (number of
342 control variables) \times 175 \times 166 \times 40 (number of grid cells)) elements. Thus, it
343 is necessary to mathematically treat and approximately simplify B to facilitate
344 numerical calculations. Following the method used by Li et al. (2013) and
345 Zang et al., (2016), B is decomposed into a background-error SD matrix and a
346 background-error correlation coefficient matrix for calculations. (2) As the
347 true value of B is unknown, it is necessary to develop a reasonable statistical
348 method to estimate it. The National Meteorology Center (NMC) method
349 (Parrish and Derber, 1992) is employed in this study to statistically estimate B .
350 Specifically, the differences between 48h and 24h forecasts of control
351 variables are assumed to be a proxy of background error. Then, B is estimated
352 based on the covariance of the difference field, which is obtained by
353 producing continuous 24h and 48h forecasts for a month using the
354 WRF–Chem model.

355 **2.5. Observation forward operator and its adjoint**

356 The observation forward operator involves two steps of calculation. (1)
357 The control variables at each grid cell are mapped to the observation space,
358 i.e., the control variables are mapped to AEC values (or $PM_{2.5}$ and PM_{10} MCs).
359 (2) The mapped values at the eight vertices of the model grid cell associated
360 with the observation data are interpolated using the inverse distance-weighted
361 method to the observation location. Here we only describe the first step of the
362 observation operators which is different for different observation data.

363 The AEC observation operator is based on the IMPROVE equation. The
364 following shows the specific form of the IMPROVE equation:

$$\begin{aligned} Ext = & 3.025 \times fs(RH) \times [Small\ Sulfate] + \\ & 6.6 \times fl(RH) \times [Large\ Sulfate] + \\ & 3.096 \times fs(RH) \times [Small\ Nitrate] + \\ & 6.579 \times fl(RH) \times [Large\ Nitrate] + \\ & 5.04 \times [Small\ Organic\ Mass] + \\ & 10.98 \times [Large\ Organic\ Mass] + \\ & 10.0 \times [Elemental\ Carbon] + \end{aligned} \quad (2)$$

$$1.0 \times [Fine\ Soil] +$$

$$1.7 \times f_{ss}(RH) \times [Sea\ Salt] +$$

$$1.0 \times [Coarse\ Mass]$$

365 The left side of Equation (2) is the AEC value Ext (unit: 10^{-6} m^{-1}). The
 366 variables in the brackets on the right side of Equation (2) are combinations of
 367 the 16 control variables (unit: $\mu\text{g}/\text{m}^3$). The coefficient variables $f_s(RH)$, $f_l(RH)$,
 368 and $f_{ss}(RH)$ reflect the effects of hygroscopicity of fine, coarse, and sea-salt
 369 aerosols in various relative humidity (HR) conditions on extinction efficiency,
 370 respectively. The values of parameters given by Gordon et al. (2018) are used
 371 in this study. The variables (in the square brackets) at each grid cell are
 372 obtained by combining the 16 control variables using the following method:

$$Sulfate = SO_{4,2.5} + \alpha \times NH_{4,2.5}$$

374 The principle for determining α is: $NH_{4,2.5}$ is preferentially allocated to
 375 $SO_{4,2.5}$, and the remaining $NH_{4,2.5}$ is allocated to $NO_{3,2.5}$.

$$376 \quad [Small\ Sulfate] = \begin{cases} 0 & , Sulfate \geq 20 \\ (1 - \frac{Sulfate}{20}) \times Sulfate & , Sulfate < 20 \end{cases}$$

$$377 \quad [Large\ Sulfate] = Sulfate - [Small\ Sulfate]$$

$$378 \quad Nitrate = NO_{3,2.5} + (1 - \alpha) (NH_{4,2.5})$$

$$379 \quad [Small\ Nitrate] = \begin{cases} 0 & , Nitrate \geq 20 \\ (1 - \frac{Nitrate}{20}) \times Nitrate & , Nitrate < 20 \end{cases} \quad (3)$$

$$380 \quad [Large\ Nitrate] = Nitrate - [Small\ Nitrate]$$

$$381 \quad [Organic\ Mass] = OC_{2.5}$$

$$382 \quad [Small\ Organic\ Mass] = \begin{cases} 0 & , [Organic\ Mass] \geq 20 \\ (1 - \frac{[Organic\ Mass]}{20}) \times [Organic\ Mass] & , [Organic\ Mass] < 20 \end{cases}$$

$$383 \quad [Large\ Organic\ Mass] = [Organic\ Mass] - [Small\ Organic\ Mass]$$

$$384 \quad [Elemental\ Carbon] = EC_{2.5}$$

$$385 \quad [Fine\ Soil] = OIN_{2.5}$$

$$386 \quad [Sea\ Salt] = CL_{2.5} + NA_{2.5}$$

$$387 \quad [Coarse\ Mass] = SO_{4,2.5-10} + NO_{3,2.5-10} + NH_{4,2.5-10} + OC_{2.5-10} +$$

$$388 \quad EC_{2.5-10} + CL_{2.5-10} + NA_{2.5-10} + OIN_{2.5-10}$$

389 The observation operator for each of $PM_{2.5}$ and PM_{10} is the sum of
 390 control variables in the corresponding particle-size bin, i.e.,

$$391 \quad PM_{2.5} = SO_{4,2.5} + NO_{3,2.5} + NH_{4,2.5} + OC_{2.5} + EC_{2.5} + CL_{2.5} + NA_{2.5} + OIN_{2.5} \quad (4)$$

$$392 \quad PM_{10} = SO_{4,2.5} + NO_{3,2.5} + NH_{4,2.5} + OC_{2.5} + EC_{2.5} + CL_{2.5} + NA_{2.5} + OIN_{2.5} +$$

393 $SO_{4,2.5-10}+NO_{3,2.5-10}+NH_{4,2.5-10}+OC_{2.5-10}+EC_{2.5-10}+CL_{2.5-10}+NA_{2.5-10}+OIN_{2.5-10}$ (5)

394 The corresponding adjoint operators for PM and AEC are developed and
395 passed the adjoint sensitivity test. The adjoint test method please refer Zou et
396 al.(1997).

397 **2.6. DA and forecast experimental design and verification analysis method**

398 To analyze the effects of DA on aerosol analysis and forecasts, one
399 control experiment with unassimilated data and three DA experiments are
400 designed for a pollution event that occurred from November 13 to 14, 2018
401 (Table 1). In the control experiment, no chemical observation data are
402 assimilated. Forecasts are produced for a 36-h period, starting at 0000 UTC on
403 November 13, 2018. In the DA experiments, hourly aerosol data for the period
404 0000–1200 UTC on November 13, 2018 are assimilated. Then with the
405 analysis field obtained from DA as the initial chemical field, forecasts are
406 performed for a 24-h period starting at 1200 UTC on November 13, 2018. The
407 period 0000–1200 UTC on November 13, 2018 is set as DA period. For the
408 DA period, the first DA (0000 UTC on November 13, 2018) is performed with
409 the initial field of the control experiment as the background field. By
410 assimilating the observation data for 0000 UTC on November 13, 2018, a DA
411 analysis field is generated for this time point. With this DA analysis field as
412 the initial field at 0000 UTC, November 13, 2018 in the DA experiment, 1-h
413 forecasts are produced. And the forecasts produced for 0100 UTC, November
414 13, 2018 are used as the background field for the second DA. The process is
415 repeated until 13 assimilation cycles are completed. Thus, a DA analysis field
416 for 1200 UTC, November 13, 2018 is generated. The period from 1200 UTC,
417 November 13, 2018 to 1200 UTC, November 14, 2018 is selected to compare
418 model forecasts. The effects of DA on forecast performance can be analyzed
419 by comparing the DA and control experiments in terms of forecast
420 performance. The three DA experiments differ in assimilated data. In the first
421 DA experiment (DA_PM), PM data alone are assimilated. In the second DA

422 experiment (DA_Ext), lidar data alone are assimilated. In the third DA
423 experiment (DA_PM_Ext), PM and lidar data are assimilated simultaneously.
424 Furthermore, $0.25^\circ \times 0.25^\circ$ 6-h reanalysis data provided by the U.S. National
425 Centers for Environmental Prediction (NCEP) are used as the meteorological
426 field of the model.

427 Two metrics, namely, regional mean and root-mean-square error (RMSE),
428 are used to evaluate simulation and forecast accuracy for PM_{2.5}MCs in the
429 experiments. The closer the mean of simulated values is to the mean of
430 measurements and the smaller the RMSE is, the higher the performance is. Let
431 M_i , O_i , N , \bar{M} , and \bar{O} be the simulated value sample, the measured value
432 sample, the number of samples, the mean of simulated values, and the mean of
433 measurements, respectively. The following summarizes the equation for
434 calculating each metric:

$$435 \quad \bar{M} = \frac{1}{N} \sum_{i=1}^N M_i \quad (6)$$

$$436 \quad \bar{O} = \frac{1}{N} \sum_{i=1}^N O_i \quad (7)$$

$$437 \quad \text{RMSE} = \sqrt{\frac{1}{N} \sum_{i=1}^N (M_i - O_i)^2} \quad (8)$$

438 3. Results

439 3.1. SD and vertical correlation coefficient of the background error 440 (BESD and BEVCC)

441 Under the same conditions, the larger the BESD is, the greater the
442 increment caused by DA is. Therefore, the structural pattern of the BESD will
443 significantly affect the distribution pattern of the DA increment field. Figure 2
444 shows the vertical BESD profiles of the 16 control variables. As demonstrated
445 in Figure 2, the BESD differs relatively significantly between control variables.
446 The seven control variables with the largest BESDs below the height of 1,000
447 m (corresponding to the 22nd layer of the model) in descending order of BESD
448 are: OIN_{2.5-10}, NO₃_{2.5}, OIN_{2.5}, NH₄_{2.5}, SO₄_{2.5}, OC_{2.5}, and EC_{2.5}. As height



449 increases, the BESD of each control variable decreases. The rates of increase
450 are the highest above the boundary layers at heights of 1,000–2,000 m
451 (corresponding to the 20th–25th layers of the model).

452 The BEVCC matrix can affect the vertical transference range of
453 observation information. Even the PM data are only available at surface, there
454 will still be DA increments of PM in near-surface in-air after PM DA.
455 Similarly, even no near-surface lidar data are available, assimilating lidar data
456 can still correct the surface PM_{2.5}MC distribution. Figure 3 shows the BEVCC
457 matrices of six control variables with relatively large BESDs (OIN_{2.5-10},
458 NO₃_{2.5}, OIN_{2.5}, NH₄_{2.5}, SO₄_{2.5}, and OC_{2.5}). As demonstrated in Figure 3, the
459 BEVCCs of the control variables share certain common characteristics. The
460 correlation decreases as the interlayer spacing of the model increases. Each
461 in-air layer is positively correlated with the surface layer, though the
462 correlation decreases as height increases. OIN_{2.5-10} has a significantly weaker
463 vertical correlation than the other variables. For OIN_{2.5-10}, the correlation
464 coefficient between the surface and 10th layers is 0.34, compared with
465 0.49–0.51 for other variables. This is mainly because coarse particles settle
466 faster than fine particles and are concentrated near the surface in larger
467 quantities.

468 **3.2. Analysis of the pollution process**

469 Figure 4 shows the evolutionary process of surface PM_{2.5}MC
470 measurements and the NCEP reanalysis surface wind field in the D02 region
471 for the period from 0000 UTC, November 13, 2018 to 1200 UTC, November
472 14, 2018 (the time interval between Figure 4a, b, c, and d is 12 h). As
473 demonstrated in Figure 4a, at 0000 UTC on November 13, 2018, the D02
474 region was predominantly controlled by a high-pressure circulation centered
475 over Zibo in central Shandong province. There was a clockwise wind field
476 around the high-pressure center. There were northerlies (easterlies) east (south)

477 of the high-pressure center, bringing clean air over the sea landward. As a
478 result, PM_{2.5}MCs in East China were relatively low. For example, the mean
479 PM_{2.5}MC measured at the ground environmental monitoring stations in
480 Nanjing, Jiangsu province, was 41.8 μg/m³. There were relatively slow
481 southerlies west and northwest of the high-pressure center. This led to
482 favorable conditions for pollutant accumulation east of the Taihang Mountains
483 and south of the Yan Mountains. As a result, North China was relatively
484 heavily polluted by PM_{2.5}. For example, the mean PM_{2.5}MCs in Beijing and
485 Shijiazhuang, Hebei Province, were 122.7 and 149.3 μg/m³, respectively. In
486 addition, within the region, there was also a northeast–southwest-trending cold
487 front near Buyant-Ovoo–Bayan-Ovoo in Mongolia. As time passed (Figure 4b,
488 c, and d), the high-pressure center gradually moved northeastward and had
489 reached near the eastern boundary of the region by 1200 UTC, November 14,
490 2018 (Figure 4d). The cold front gradually moved southeastward and had
491 reached the Chaoyang–Beijing–Taiyuan–Xi’an line by 1200 UTC, November
492 14, 2018 (Figure 4d). As the high-pressure center and the cold front moved,
493 the level of pollution in North China continued to rise, and pollution gradually
494 expanded northeastward (Chaoyang, Liaoning Province), southward
495 (Zhengzhou, Henan Province), and westward (Taiyuan, Shanxi Province). Due
496 to the dual action of the advective transport by easterlies and the narrow
497 terrain, the level of pollution gradually increased in the Wei and Yellow River
498 Valleys east of Xi’an, Shaanxi Province. Thanks to good dispersion conditions,
499 PM_{2.5}MCs decreased considerably upon the passing of the cold front. There
500 were no significant changes in PM_{2.5}MCs in East China, owing to the
501 continuous impact of sea winds.

502 3.3. Analysis of the direct affects of DA

503 Figure 5 shows the AEC profiles captured at four lidar stations at 0000
504 UTC, November 13, 2018 as well as the corresponding AEC profiles in the

505 analysis fields of the control and DA experiments and the simulated RH
506 profiles. The first DA is performed for 0000 UTC, November 13, 2018. The
507 results of the control experiment are used as the background field in the three
508 DA experiments. Figure 5a, b, c, and d show the results for Beijing,
509 Shijiazhuang, Taiyuan, and Wuhu, respectively. As demonstrated by the RH
510 profiles (brown lines) in Figure 5, the RH in air below 1 km is basically
511 consistent with the surface RH. Thus, vertical changes in AEC values below 1
512 km are relatively insignificantly affected by RH, and the AEC profiles can
513 describe vertical changes in PM_{2.5}MC profiles. A comparison of lidar AEC
514 profiles (black lines) and those obtained from the control experiment (blue
515 lines) finds that AEC values obtained from the control experiment are
516 relatively underestimated for Shijiazhuang (Figure 5b) and Taiyuan (Figure
517 5c), particularly near the height of 100 m (starting height for lidar data). In
518 comparison, AEC values for Wuhu (Figure 5d) obtained from the control
519 experiment are higher than the lidar measurements, while the AEC profile for
520 Beijing (Figure 5a) obtained from the control experiment is in relatively good
521 agreement with the lidar AEC profile. The AEC values for the Beijing (Figure
522 5a), Taiyuan (Figure 5c), and Wuhu (Figure 5d) stations obtained from the
523 DA_PM experiment (green lines) based on assimilated surface PM MC
524 measurements are lower than those obtained from the control experiment. This
525 is because the surface PM MC measurements used in the control experiment
526 for these three stations are relatively high. As a result of the BEVCC (Figure
527 3), PM DA will reduce the AEC values in lower in-air layers while reducing
528 surface PM MCs. In the DA_PM experiment, the adjustment made to the AEC
529 profiles for Beijing and Wuhu is, overall, positive, but the adjustment made to
530 the AEC profile for Taiyuan increases the underestimation of in-air AEC
531 values.

532 Compared to the DA_PM experiment, vertical aerosol distribution
533 patterns obtained from the DA_Ext experiment (purple lines) are more finely



534 adjusted. For example, the AEC values obtained from the DA_Ext experiment
535 for the Taiyuan station (Figure 5c) for the heights of approximately 100 and
536 700 m are significantly higher than those obtained from the DA_PM
537 experiment and are consistent with those on the lidar AEC profile (black line).
538 The AEC profile obtained from the DA_Ext experiment for the Wuhu station
539 (Figure 5d) is very close to the lidar AEC profile. This suggests that the AEC
540 observation operator designed based on the IMPROVE equation effectively
541 facilitates 3D variational assimilation of lidar AEC data. In addition, due to
542 the BEVCC (Figure 3), lidar DA will increase (decrease) surface PM MCs
543 while increasing (decreasing) in-air PM MCs. This surface PM MC
544 adjustment effectively corrects the overestimation of surface PM_{2.5}MCs in
545 Beijing and Wuhu in the control experiment but increases the overestimation
546 of surface PM_{2.5}MCs in Taiyuan.

547 The in-air AEC profiles obtained from the DA_PM_Ext experiment (red
548 lines) for the four cities almost coincide with those obtained from the DA_Ext
549 experiments above 400 m. The near-surface AEC values obtained from
550 DA_PM_Ext experiment for Beijing (Figure 5a) almost coincide with those
551 obtained from the DA_PM experiment. The near-surface AEC values obtained
552 from DA_PM_Ext experiment for Taiyuan (Figure 5c) are between those
553 obtained from the DA_PM and DA_Ext experiments. The near-surface AEC
554 values obtained from DA_PM_Ext experiment for Wuhu (Figure 5d) are
555 lower than those from the DA_PM and DA_Ext experiments. This suggests
556 that simultaneously assimilating two types of data can fully integrate their
557 observation information and reflect their respective advantages and, on this
558 basis, generate the most accurate analysis field.

559 Figure 6 shows the AEC profiles at 1200 UTC, November 13, 2018
560 measured at four lidar stations as well as the corresponding AEC profiles
561 obtained from the control experiment and the background and analysis fields
562 of the DA experiments. A total of 13 DA cycles are performed for the period

563 00:00–12:00 UTC, November 13, 2018. The time of 1200 UTC, November 13,
564 2018 is the last time point of the DA period and the starting time point of the
565 forecast period. The background field for each of the three DA experiments is
566 generated during the continuous DA period, whereas the results of the control
567 experiment are obtained by forecasting starting at 0000 UTC, November 13,
568 2018. As a result, there is a relatively significant difference between the
569 background fields of the three DA experiments and the results of the control
570 experiment.

571 As demonstrated in Figure 6, the results of the DA_PM experiment
572 (green lines) show significant PM_{2.5}MC increments below 1 km. The problem
573 of near-surface overestimation for the four cities in the control experiment is
574 corrected in the DA_PM experiment. This suggests that the DA yields a
575 positive effect. However, compared to those from the control experiment, the
576 AEC values obtained from the DA_PM experiment for Taiyuan at heights of
577 120–400 m (Figure 6c) and Wuhu above 400 m (Figure 6d) are even more
578 underestimated, suggests that the DA yields a negative effect here. It is worth
579 noting that there are very small direct DA increments (i.e., the differences
580 between the solid and dotted green lines) generated in the DA_PM experiment
581 at this time point. This means that for surface PM DA, a DA period of 11 h or
582 less is sufficient to effectively adjust aerosol distribution. This is because
583 aerosols are primarily concentrated near the surface and surface PM data cover
584 a wide area and have a high spatial resolution, so surface PM data measured at
585 a few time points contain the main aerosol distribution information for the
586 whole region.

587 Compared to the DA_PM experiment, the DA_Ext experiment (purple
588 lines) reflects the advantages of AEC DA in adjusting vertical aerosol
589 distribution. The problem of overestimation for Beijing above 300 m (Figure
590 6a), Taiyuan above 600 m (Figure 6c), and Wuhu below 400 m (Figure 6d) in
591 the control experiment is effectively corrected in the DA_PM experiment. In



592 addition, the results of the DA_Ext experiment reflect the rapid decrease in
593 $PM_{2.5}MC$ with a height below 1 km in Beijing (Figure 6a) and the presence of
594 a maximum- $PM_{2.5}MC$ layer at the height of 1.3 km in Wuhu (Figure 6d).
595 However, the near-surface overestimation for Taiyuan (Figure 6c) is increased
596 in the DA_Ext experiment. Moreover, the direct DA increments (i.e., the
597 differences between the solid and dotted purple lines) generated in the
598 DA_Ext experiment at this time point remain notable. This suggests that the
599 error of the background field at each lidar station at 1200 UTC on November
600 13, 2018 remains relatively large, even after a continuous DA period of 12 h.
601 To improve the effects of DA, it is necessary to increase the length of the
602 continuous DA period. This may be because there are few lidars and the lidars
603 are relatively far apart from one another. As a result, the simulation error for
604 the region upstream of the lidar is difficult to be corrected through DA and
605 will affect the lidar locate under advection at the next time point.

606 The AEC profiles obtained from the DA_PM_Ext experiment (solid red
607 lines) compared to the other two DA experiments show that the problem of
608 overestimation for Beijing above 400 m (Figure 6a), Shijiazhuang above 300
609 m (Figure 6b), and Wuhu in the near-surface layer (Figure 6d) in the control
610 experiment is considerably corrected in the DA_PM_Ext experiment. The
611 results of the DA_PM_Ext experiment reflect the advantage of simultaneously
612 assimilating two types of data in integrating their observation information.
613 This finding is consistent with Figure 5.

614 Figure 7 shows the surface $PM_{2.5}MC$ s measured at 1200, November 13,
615 2018 as well as the corresponding initial field of the control experiment and its
616 error and the distribution of differences between the initial fields of the control
617 and DA experiments. As demonstrated in Figure 7a and 7b, the simulation
618 results obtained from the control experiment show that $PM_{2.5}MC$ s are
619 relatively high in North China. In particular, there is a heavily polluted zone in
620 the Beijing–Shijiazhuang–Zhengzhou region, and $PM_{2.5}MC$ s are relatively low



621 in the region surrounding North China. However, as demonstrated in Figure 7c,
622 PM_{2.5}MCs obtained from the control experiment are overestimated for most
623 regions. In particular, PM_{2.5}MCs obtained from the control experiment are
624 relatively highly overestimated for the Beijing–Shijiazhuang–Zhengzhou
625 region. In comparison, PM_{2.5}MCs obtained from the control experiment are
626 underestimated for the region near Chaoyang, Liaoning Province. The
627 distribution trends in Figure 7c and d are relatively consistent. This indicates
628 that the overestimation for most regions and the underestimation for some
629 regions in the initial field of the control experiment are corrected by PM DA.
630 As a result, the analysis field of the DA_PM experiment is closer to the
631 measurements.

632 A comparison of Figure 7c and 7e finds that significant DA increments
633 are generated in the DA_Ext experiment in the regions surrounding the five
634 lidar stations and the regions downstream of the wind field (Figure 4). Certain
635 DA increments are also present in regions far away from the lidar stations.
636 This indicates that long-term continuous assimilation of lidar measurements
637 can affect a relatively large area. Overall, AEC DA (from the DA_Ext
638 experiment) corrects the overestimation for most regions and the
639 underestimation for some regions in the initial field of the control experiment.
640 However, DA increments on the surface generated in the DA_Ext experiment
641 are smaller than those generated in the DA_PM experiment in terms of
642 horizontal spatial range and magnitude. This is mainly because there are
643 relatively few lidars and these lidars cover a limited spatial area. It is worth
644 noting that AEC DA yields a negative effect for northern Beijing and the
645 region around Taiyuan. For northern Beijing, the negative effect results
646 primarily from the notable overestimation for the location of the Beijing lidar
647 station, whereas the overestimation for northern Beijing is relatively low, and
648 there is even an underestimation for the locations of some individual stations
649 north of Beijing (Figure 7c). As a result, a negative effect is generated after



650 the DA increment at the location of the lidar station is transferred to northern
651 Beijing. For Taiyuan, the cause of the negative effect is similar to that seen in
652 Figure 5. According to the lidar measurements, the observation background
653 error at the height of approximately 100 m in the control experiment is
654 positive, i.e., there is an underestimation. However, according to the surface
655 PM MC measurements, the surface observation background error in the
656 control experiment is negative, i.e., there is an overestimation. Due to the
657 impact of the BEVCC, lidar DA will increase surface PM MCs while
658 increasing in-air PM MCs. This will lead to an increased overestimation of
659 surface PM MCs. There are two reasons for the presence of opposite in-air and
660 surface observation background errors. On the one hand, the simulation error
661 of the model is nonuniform in the vertical direction. On the other hand, the
662 opposite errors may be because the observation information in the lidar and
663 PM data was obtained from air parcels differing relatively significantly in
664 PM_{2.5}MCs in the horizontal direction. PM_{2.5}MCs measured at 1200 UTC,
665 November 13, 2018 at three ground environmental monitoring stations within
666 6 km of the Taiyuan lidar station were 80.0, 137.0, and 146.0 μg/m³,
667 respectively. As also demonstrated in Figure 7a, PM_{2.5}MC measurements were
668 relatively low at most stations near Taiyuan (blue) but very high at two
669 stations (red). A similar phenomenon can be observed for the measurements
670 taken between 0000 and 1100 UTC. This suggests a relatively large horizontal
671 PM_{2.5}MC gradient near Taiyuan. The lidar and ground environmental
672 monitoring stations were situated at different locations. This led to a relatively
673 significant difference in PM_{2.5}MC data acquired in air parcels at the lidar and
674 ground environmental monitoring stations. All of this suggests that particular
675 attention should be paid to the horizontal spatial representativeness of lidar
676 data during the DA process.

677 A comparison of the results of the three DA experiments finds that the
678 results of the DA_PM_Ext experiment are in relatively good agreement with



679 those of the DA_PM experiment. This is mainly because the PM data are far
680 greater than the lidar data in terms of quantity and spatial coverage. As a result,
681 the DA increments in surface PM_{2.5} concentrations originate primarily from
682 the observation information in the PM data. However, by analyzing Figures 5
683 and 6, it can be reasonably inferred that as height increases, the analysis field
684 of the DA_PM_Ext experiment will include more observation information in
685 the lidar data and thereby more accurately reflect the 3D spatial distribution
686 pattern of aerosols.

687 **3.4. Effects of DA on the forecast performance for surface PM_{2.5}MCs**

688 In this section, the effects of DA on forecast performance for aerosols are
689 evaluated based on approximately 430 surface PM_{2.5}MC measurements that
690 cover most of the D02 region.

691 Figure 8 shows the trend of the variation in the regional mean PM_{2.5}MC
692 with time in each of the four experiments. As demonstrated in Figure 8, the
693 variation in PM_{2.5}MC measurements (black line) exhibits a notable diurnal
694 pattern. Two notable minimum PM_{2.5}MCs (69.1 and 77.9 µg/m³) appeared at
695 0800 UTC (1600 local time), November 13, 2018 and 0800 UTC (1600 local
696 time), November 14, 2018, respectively. High PM_{2.5}MCs appeared between
697 1300 UTC, November 13, 2018 and 0200 UTC, November 14, 2018 (from
698 night to morning). The maximum PM_{2.5}MC was 96.0 µg/m³. However, there
699 was a relative minimum PM_{2.5}MC (87.0 µg/m³) appearing at 2200 UTC,
700 November 13, 2018 (around dawn local time) during the high-PM_{2.5}-MC
701 period. Comparing the control experiment with the measurements finds that
702 the experiment simulates the periodic variation pattern of the mean PM_{2.5}MC
703 (solid blue line). However, PM_{2.5}MCs obtained from the control experiment
704 are significantly overestimated for the whole forecast period. The PM_{2.5}MC
705 obtained from the control experiment for the initial time point (1200 UTC,
706 November 13, 2018) is overestimated by 36.3 µg/m³ (39.3%).



707 The overestimation in the control experiment is significantly reduced in
708 the DA_PM experiment (green line, which, partially, almost coincides with
709 the red line). The mean PM_{2.5}MC obtained from the DA_PM experiment for
710 1200 UTC, November 13, 2018 (91.4 µg/m³) is lower than that obtained from
711 the control experiment (128.6 µg/m³) by 37.2 µg/m³ (28.9%) and is closer to
712 the measurement (92.3 µg/m³). As a result of the decrease in the MC level in
713 the initial field, the PM_{2.5}MC forecasts obtained from the DA_PM experiment
714 are significantly lower than those obtained from the control experiment for the
715 whole forecast period. This suggests that the overestimation of the initial field
716 is the primary cause of the overestimated forecasts obtained from the control
717 experiment. In addition, DA can improve forecast results over a long time by
718 optimizing the initial field. In the DA_PM experiment, the effects of PM DA
719 last for more than 24 h. As demonstrated by the results of the DA_Ext
720 experiment (purple line), while there are only five lidars within the region,
721 AEC DA can still significantly correct the overestimation error of the initial
722 field and improve forecast performance. Compared to those in the DA_PM
723 experiment, the DA increments generated in the DA_Ext experiment are
724 relatively small and affect forecast results for a relatively short time
725 (approximately 21 h). This is mainly a result of the relatively small number of
726 lidars. There was no significant difference between the results of the
727 DA_PM_Ext (red line) and DA_PM (green line) experiments at surface. This
728 suggests that after surface PM DA, lidar DA relatively insignificantly affects
729 surface PM_{2.5}MCs. This happens for two reasons. On the one hand, similar to
730 the analysis of Figure 7f, of the two types of assimilated data, the proportion
731 of PM data is far greater than that of lidar data. On the other hand, after
732 surface PM DA, lidar DA affects surface aerosol forecasts mainly by adjusting
733 in-air AMCs and, on this basis, indirectly affects surface AMC forecasts by
734 processes such as settling. However, in this simulation process, surface AMC
735 remains at relatively high levels. Moreover, due to the relatively stable



736 meteorological conditions and weak vertical air movement in the simulation
737 region, particularly the heavily polluted zone, the indirect effects of lidar DA
738 are far smaller than the direct effects of PM DA on surface AMCs.

739 Figure 9 shows the variation in the RMSE of surface PM_{2.5}MC forecasts
740 with time. A comparison of the RMSEs from the control experiment (blue line)
741 in Figure 9 and the mean PM_{2.5}MCs obtained from the control experiment in
742 Figure 8 finds that the RMSEs for simulations and forecasts are relatively
743 large (small) at a relatively high (low) aerosol pollution level. As
744 demonstrated in Figure 9, the RMSE in the control experiment for the initial
745 time point (1200 UTC, November 13, 2018) of the forecast period is 59.6
746 $\mu\text{g}/\text{m}^3$. Throughout the forecast period, the RMSE fluctuates between 44.5 and
747 $67.1 \mu\text{g}/\text{m}^3$, instead of linearly increasing or decreasing. The RMSEs from the
748 DA_PM (green line), DA_Ext (purple line), and DA_PM_Ext (red line)
749 experiments for the initial time point are 21.0, 49.1, and $21.2 \mu\text{g}/\text{m}^3$,
750 respectively, which are 38.6 (64.8%), 10.5 (17.6%), and $38.4 \mu\text{g}/\text{m}^3$
751 lower than that for the control experiment. This suggests that the error of the
752 initial field is reduced in each of the three DA experiments. Thanks to an
753 optimized initial field, the RMSE of the forecasts produced in each of the DA
754 experiments is lower than that for the forecasts produced in the control
755 experiment. The RMSEs of the forecasts produced in the Da_PM, Da_Ext,
756 and DA_PM_Ext experiments for the 24th forecast hour are 6.1 (11.8%), 1.5
757 (2.9%), and $6.5 \mu\text{g}/\text{m}^3$ smaller than that of the forecast produced in
758 the control experiment, respectively. This suggests that the optimization of the
759 initial field has a lasting (more than 24 h in all cases) positive effect on model
760 forecasts. It is worth noting that while there are very few lidar stations, the
761 results of the DA_Ext experiment are still better than those of the control
762 experiment, and the results of the DA_PM_Ext experiment are also slightly
763 better than those of the DA_PM experiment. This indicates that even in
764 relatively low quantities, lidar data still improve the forecast performance of



765 the model. As lidar data become increasingly rich and provide more vertical
766 and horizontal aerosol distribution information in future, lidar DA will further
767 improve PM_{2.5}MC forecasts.

768 **4. Discussion**

769 In Figure 7e, the relatively large AMC gradient in Taiyuan leads to
770 opposite in-air and surface observation background errors, which lead to a
771 negative effect of lidar DA for the surface. This suggests that the spatial
772 representativeness of lidar data relatively significantly affects the impact of
773 lidar AEC DA. In addition, the vertical resolution of lidar data (smaller than
774 15 m) is far smaller than the spacing between adjacent height layers of the
775 model. As a result, the representative spatial scale of original lidar data does
776 not match the resolution of the model. To improve the horizontal spatial
777 representativeness of the lidar data, the lidar data of the past hour are averaged
778 in this experiment as the lidar AEC profile for the time point. The vertical
779 spatial representativeness of the data is improved by smoothing over 30 m in
780 the vertical direction. However, the time-averaged lidar data represent
781 observation information for a certain area downstream of the wind field. This
782 representativeness error needs addressing in subsequent studies. Moreover,
783 selection of a time averaging window length and a vertical smoothing length
784 also requires further investigation.

785 For the Beijing region in Figure 7e, as a result of the relatively significant
786 difference between the simulation error for the region downstream of the wind
787 field and that for the location of the lidar station, the downstream transference
788 of lidar DA increments will cause a negative effect in the continuous DA
789 process. The most direct and effective measure for addressing this problem is
790 to increase the number of lidars and the coverage of lidar network. This
791 measure will ensure that the simulation error for the simulation region will be
792 more comprehensively captured. However, lidar detection requires great



793 amounts of labor and financial resources. Therefore, it is difficult to arrange
794 lidar stations as densely as ground environmental monitoring stations. A
795 relatively feasible method is to set a relatively small number of lidars in
796 regions with relatively small spatial changes in the simulation error and set
797 dense lidars in regions with significant spatial changes in the simulation error.
798 This will make it possible to use the limited number of lidars to capture more
799 useful information. Thus, studying the temporal and spatial distribution pattern
800 of model simulation errors can provide a useful reference for future
801 arrangement and planning of lidar stations. This merits further investigation.

802 The AEC observation operator used in this study is designed based on the
803 IMPROVE equation. The parameters of the IMPROVE equation, such as
804 hygroscopicity coefficient, are directly set to values reported in previous
805 studies. On the one hand, datasets used in previous studies were measured in
806 specific regions. To date, no quantitative comparative analysis has yet to be
807 performed to determine whether the extinction properties of aerosols differ
808 between regions. Therefore, there is some uncertainty in the applicability of
809 the IMPROVE equation. On the other hand, the values of the coefficients in
810 the IMPROVE equation are determined by extensive statistical analysis of
811 data. This dictates that these coefficients represent average levels under certain
812 pollution and humidity conditions. There may be a certain error in these
813 coefficients when applied to a specific observation event. This error will
814 accumulate and amplify during the calculation of the forward and reverse
815 processes of the observation operator, resulting in a negative effect of DA.
816 Hence, how to effectively evaluate the applicability of the IMPROVE
817 equation and more accurately adjust its coefficients is another issue that needs
818 addressing.

819 **5. Conclusions**



820 In this study, an observation operator and its adjoint is designed based on
821 the IMPROVE equation to facilitate 3-DVAR assimilation of AEC data and a
822 3-DVAR DA system is developed for lidar AEC data and surface AMC data
823 for the MOSAIC-4bin chemical scheme in the WRF–Chem model. Three DA
824 experiments (i.e., a $PM_{2.5}(PM_{10})$ DA experiment, a lidar AEC DA experiment,
825 and a simultaneous $PM_{2.5}(PM_{10})$ and lidar AEC DA experiment) are conducted
826 based on AEC profiles captured by five lidars (located in Beijing,
827 Shijiazhuang, Taiyuan, Xuzhou, and Wuhu) in the period from 0000 to 1200
828 UTC, November 13, 2018 as well as MC measurements for $PM_{2.5}$ and PM_{10}
829 taken at over 1,500 ground environmental monitoring stations across China.
830 DA and forecast results are evaluated based on MC measurements for surface
831 $PM_{2.5}$. A comparison with the control experiment involving no DA finds that
832 the 3-DVAR DA system is effective at assimilating lidar AEC data. While
833 there are only five lidars within the simulation region (approximately 2.33
834 million km^2 in size), assimilating AEC data acquired by these lidar alone can
835 also effectively improve the accuracy of the initial field and the forecast
836 performance of the model for $PM_{2.5}$. Moreover, the positive effect resulting
837 from the optimization of the initial field on forecast performance for $PM_{2.5}$ can
838 last for more than 24 h. Lidar AEC DA is advantageous because it improves
839 the accuracy of the vertical $PM_{2.5}MC$ profile. Surface $PM_{2.5}(PM_{10})$ DA is
840 advantageous because it optimizes the near-surface $PM_{2.5}MC$ distribution.
841 Furthermore, simultaneous lidar AEC and surface $PM_{2.5}(PM_{10})$ DA can
842 effectively help integrate their observation information to generate a more
843 accurate 3D aerosol analysis field.

844

845 **Code and data availability:** WRF-Chem model source code can be download
846 at the WRF model download page ([https://www2.mmm.ucar.edu/wrf/users/
847 download/get_source.html](https://www2.mmm.ucar.edu/wrf/users/download/get_source.html)). This 3-DVAR data assimilation system is
848 developed by myself. A version of the 3-DVAR code and lidar profile data for



849 supporting this paper are available at: <https://zenodo.org/record/3937564>.
850 Full access is available on request from the corresponding author
851 (ywlx_1987@163.com)

852 **Author contribution:** Yanfei Liang performed numerical experiments, data
853 analysis and wrote the initial manuscript. Yanfei Liang, Zengliang Zang and
854 Wei You developed the 3-DVAR data assimilation system, designed this study
855 and revised the manuscript. Zengliang Zang supervised the project of
856 development. All the authors continuously discussed the 3-DVAR system
857 development and the results of the manuscript.

858 **Competing interests:** The authors declare that they have no conflict of
859 interest.

860 **Acknowledgments**

861 This research was primarily supported by the National Natural Science
862 Foundation of China (Grant No.41775123 and No.41805092), the National
863 Key Research and Development Program of China(Grant No.
864 2017YFC0209803). We thank the China National Environmental Monitoring
865 Center (CNEMC) for providing PM_{2.5} and PM₁₀ data through the website
866 (<http://www.cnemc.cn/>).

867

868 **References:**

869 Bannister, R. N., 2017: A review of operational methods of variational and
870 ensemble-variational data assimilation. *J. Quarterly Journal of the Royal*
871 *Meteorological Society*, 143,607-633.

872 Baraskar, A., Bhushan, M., Venkataraman, C., Cherian, R., 2016: An offline constrained
873 data assimilation technique for aerosols: improving GCM simulations over South Asia
874 using observations from two satellite sensors. *J. Atmospheric Environment*, 132, 36-48.

875 Benedetti, A., Morcrette, J. J., Boucher, Dethof, O., Engelen, R. J., Fisher, M., Flentje, H.,
876 Huneeus, N., Jones, L., Kaiser, J. W., Kinne,S., Mangold, A., Razinger, M., Simmons, A. J.,
877 Suttie, M., 2009: Aerosol analysis and forecast in the European Centre for Medium-Range

- 878 Weather Forecasts Integrated Forecast System:2. Data assimilation, *J. Journal of Geophysical*
879 *Research*, 136(5), 1727-1746.
- 880 Burton, S. P., Ferrare, R. A., Hostetler, C. A., Hair, J. W., Kittaka, C., Vaughan, M. A., Obland, M.
881 D., Rogers, R. R., Cook, A. L., Harper, D. B., Remer, L. A., 2010: Using airborne high spectral
882 resolution lidar data to evaluate combined active plus passive retrievals of aerosol extinction
883 profiles, *J. Journal of Geophysical Research Atmosphere*, 115.
- 884 Cao, J. J., Wang, Q. Y., Chow, J. C., Watson, J. G., Tie, X. X., Shen, Z. X., Wang, P., An, Z. S.,
885 2012a: Impacts of aerosol compositions on visibility impairment in Xi'an, China. *J.*
886 *Atmospheric Environment*, 59, 559–566.
- 887 Cao, J. J., Shen, Z. X., Chow, J. C., Watson, J. G., Lee, S. C., Tie, X. X., Ho, K. F., Wang, G. H.,
888 Han, Y. M., 2012b: Winter and summer PM_{2.5} chemical compositions in fourteen Chinese
889 cities. *J. Journal of the Air & Waste Management Association*, 62(10), 1214–1226.
- 890 Carmichael, G. R., Sandu, A., Chai, T., Daescu, D. N., Constantinescu, E. M., Tang, Y., 2008:
891 Predicting air quality: Improvements through advanced methods to integrate models and
892 measurements. *J. Journal of Computational Physics*, 227(7), 3540–3571.
- 893 Cheng, X. H., Liu, Y. L., Xu, X. D., You, W., Zang, Z. Z., Gao, L. N., Chen, Y. B., Su, D. B., Yan, P.,
894 2019: Lidar data assimilation method based on CRTM and WRF-Chem models and its
895 application in PM_{2.5} forecasts in Beijing. *J. Science of The Total Environment*, 682, 541-552.
- 896 Lolli, S., Welton, E. J., Benedetti, A., Jones, L., Suttie, M., Wang, S. H., 2014: MPLNET lidar data
897 assimilation in the ECMWF MACC-II Aerosol system: evaluation of model performances at
898 NCU lidar station. *C. Spie Remote Sensing*, Vol. 924601, 1-5.
- 899 Chen, Z. J., Zhang, J. S., Zhang, T. S., Liu, W. Q., Liu, J. G. 2015: Haze observations by
900 simultaneous lidar and WPS in Beijing before and during APEC, 2014 *J. Science China*, 58 (9),
901 1385–1392.
- 902 Ganguly, D., Ginoux, P., Ramaswamy, V., Dubovik, O., Welton, J., Reid, E. A., Holben, B. N., 2009:
903 Inferring the composition and concentration of aerosols by combining AERONET and
904 MPLNET data: Comparison with other measurements and utilization to evaluate GCM output.
905 *J. Journal of Geophysical Research Atmosphere*, 114, D16.
- 906 Fernald, F. G., 1984: Analysis of atmospheric lidar observations: Some comments. *J. Applied Optics*,

- 907 23, 652– 653.
- 908 Gordon T. D., Prenni A. J., Renfro J. R., McClure, E., Hicks, B., Onasch, T. B., Freedman, A.,
909 McMeeking, G. R., Chen, P., 2018: Open-path, closed-path and reconstructed aerosol
910 extinction at a rural site. *J. Journal of the Air & Waste Management Association*, 68(8),
911 824-835.
- 912 Haywood, J., and O. Boucher, 2000: Estimates of the direct and indirect radiative forcing due to
913 tropospheric aerosols: A review. *J. Reviews of Geophysics*, 38(4), 513– 543.
- 914 Jiang, Z. Q., Liu, Z. Q., Wang, T. J., Schwartz, C. S., Lin, H. C., Jiang, F., 2013: Probing into the
915 impact of 3-DVAR assimilation of surface PM10 observations over China using process
916 analysis. *J. Journal of Geophysical Research Atmospheres*, 118, 6738-6749.
- 917 Kahnert, M., 2008: Variational data analysis of aerosol species in a regional CTM: background error
918 covariance constraint and aerosol optical observation operators. *J. Tellus. Series B: Chemical
919 and Physical Meteorology*, 60(5), 753-770.
- 920 Kim, Y. J., Kim, K. W., Kim, S. D., Lee, B. K., Han, J. S., 2006: Fine particulate matter
921 characteristics and its impact on visibility impairment at two urban sites in Korea: Seoul and
922 Incheon. *J. Atmospheric. Environment*. 40(supp-S2), 593–605.
- 923 Li, Z. J., Zang, Z. L., Li, Q. B., Chao, Y., Chen, D., Ye, Z., Liu, Y., Liou, K. N., 2013: A
924 three-dimensional variational data assimilation system for multiple aerosol species with
925 WRF/Chem and an application to PM2.5 prediction. *J. Atmospheric chemistry and physics*, 13,
926 4265-4278.
- 927 Liu, Q. H., Weng, F. Z., 2006: Advanced doubling-adding method for radiative transfer in planetary
928 atmosphere. *J. Journal of the Atmospheric Sciences*, 63(12), 3459–3465.
- 929 Liu, Z., Q. Liu, Q. H., Lin, H. C., Schwartz, C. S., Lee, Y. H., Wang, T. J., 2011: Three-dimensional
930 variational assimilation of MODIS aerosol optical depth: Implementation and application to a
931 dust storm over East Asia. *J. Journal of Geophysical Research Atmosphere*, 116, D016159.
- 932 Lowenthal, D. H., Kumar, N., 2003: PM2.5 Mass and Light Extinction Reconstruction in
933 IMPROVE. *J. Journal of the Air & Waste Management Association*, 53(9), 1109-1120.
- 934 Niu, T., Gong, S. L., Zhu, G. F., Liu, H. L., Hu, X. Q., Zhou, C. H., Wang, Y. Q., 2008: Data
935 assimilation of dust aerosol observations for the CUACE/dust forecasting system. *J.*



- 936 Atmospheric Chemistry and Physics, 8(13), 3473–3482.
- 937 Parrish, D. F., and Derber, J. C., 1992: The national meteorological center’s spectral
938 statistical-interpolation analysis system. *Mon. Wea. Rev.*, 120, 1747–1763.
- 939 Peng, Z., Liu, Z. Q., Chen, D., Ban, J. M., 2017: Improving PM_{2.5} forecast over China by the joint
940 adjustment of initial conditions and source emissions with an ensemble Kalman filter. *J.*
941 *Atmospheric Chemistry and Physics*, 17(7), 4837-4855.
- 942 Pitchford, M., Maim, W., Schichtel, B., Kumar, N., Lowenthal, D., Hand, J., 2007: Revised
943 algorithm for estimating light extinction from IMPROVE particle speciation data. *J. Journal of*
944 *the Air & Waste Management Association*, 57(11), 1326-1336.
- 945 Raut, J. C., Chazette, P., 2009: Assessment of vertically-resolved PM₁₀ from mobile lidar
946 observations. *J. Atmospheric Chemistry and Physics*, 9, 8617-8638.
- 947 Roy, B., Mathur, R., Gilliland, A. B., Howard, S. C., 2007: A comparison of CMAQ-based aerosol
948 properties with IMPROVE, MODIS, and AERONET data. *J. Journal of Geophysical Research*,
949 112, D14.
- 950 Ryan, P. A., Lowenthal, D., Kumar, N., 2005: Improved Light Extinction Reconstruction in
951 Interagency Monitoring of Protected Visual Environments. *J. Journal of the Air & Waste*
952 *Management Association*, 55, 1751-1759.
- 953 Sandu, A., Chai, T., 2011: Chemical Data Assimilation—An Overview. *J. Atmosphere*, 2, 426-463.
- 954 Sekiyama, T. T., Tanaka, T. Y., Shimizu, A., Miyoshi, T., 2010: Dataassimilation of CALIPSO
955 aerosol observations, *J. Atmospheric Chemistry and Physics*, 10, 39–49.
- 956 Schwartz, C. S., Liu, Z. Q., Lin, H. C., McKeen, S. A., 2012: Simultaneous three-dimensional
957 variational assimilation of surface fine particulate matter and MODIS aerosol optical depth. *J.*
958 *Journal of Geophysical Research Atmospheres*, 117, D13.
- 959 Sugimoto, N., Matsui, I., Shimizu, A., Nishizawa, T., Yoon, S. C., 2008: Lidar network observations
960 of tropospheric aerosols. *J. Proc Spie*, 7153.
- 961 Sugimoto, N., Uno, I., 2009: Observation of Asian dust and air-pollution aerosols using a network
962 of ground-based lidars (ADNet): Realtime data processing for validation/assimilation of
963 chemical transport models. *C. WMO/GEO Expert Meeting on an International Sand and Dust*
964 *Storm Warning System*, 7, 012003.

- 965 Tang, Y. H., Pagowski, M., Chai, T. F., Pan, L., Lee, P., Baker, B., Kumar, R., Monache, L. D.,
966 Tong, D., Kim, H. C., 2017: A case study of aerosol data assimilation with the Community
967 Multi-scale Air Quality Model over the contiguous United States using 3D-Var and optimal
968 interpolation methods. *J. Geoscientific Model Development*, 10, 4743–4758.
- 969 Tao, J., Ho, K. F., Chen, L., Zhu, L., Han, J., Xu, Z., 2009: Effect of chemical composition of
970 PM_{2.5} on visibility in Guangzhou, China, 2007 spring. *J. Particuology*, 7, 68–75.
- 971 Tao, J., Cao J. J., Zhang, R. J., Zhu, L. H., Zang, T., Shi, S., Chan, C. Y., 2012: Reconstructed light
972 extinction coefficients using chemical compositions of PM_{2.5} in winter in urban Guangzhou,
973 China. *J. Advances in Atmospheric Sciences*, 29(2), 359-368.
- 974 Tao, J., Zhang, L. M., Ho, K. F., Zhang, R. J., Lin, Z. J., Zhang, Z. S., Lin, M., Cao, J. J., Liu, S. X.,
975 Wang, G. H., 2014: Impact of PM_{2.5} chemical compositions on aerosol light scattering in
976 Guangzhou-the largest megacity in South China. *J. Atmospheric Research*, 135–136, 48–58.
- 977 Tesche, M., Ansmann, A., Müller, D., Althausen, D., Engelman, R., 2007: Particle backscatter,
978 extinction, and lidar ratio profiling with Raman lidar in south and north China. *J. Applied
979 Optics*, 46(25), 6302–6308.
- 980 Tombette, M., Mallet, V., Sportisse, B., 2008: PM₁₀ data assimilation over Europe with the optimal
981 interpolation method. *J. Atmospheric Chemistry and Physics*, 9(1), 57-70.
- 982 Wang D, You W, Zang Z, Pan X, He H, Liang Y. 2020. A three-dimensional variational data
983 assimilation system for a size-resolved aerosol model: Implementation and application for
984 particulate matter and gaseous pollutant forecasts across China. *Science China Earth Sciences*,
985 63, <https://doi.org/10.1007/s11430-019-9601-4>
- 986 Wang, Y., Sartelet, K. N., Bocquet, M., Chazette, P. 2013: Assimilation of ground versus lidar
987 observations for PM₁₀ forecasting. *J. Atmospheric Chemistry and Physics*, 13, 269-283.
- 988 Wang, Y., Sartelet, K. N., Bocquet, M., Chazette, P. 2014a: Modelling and assimilation of lidar
989 signals over Greater Paris during the MEGAPOLI summer campaign. *J. Atmospheric
990 Chemistry and Physics*, 14(7), 3511-3532.
- 991 Wang, Y., Sartelet, K. N., Bocquet, M., Chazette, P., Sicard, M., Amico, G. D., Léon, J. F.,
992 Arboledas-Arboledas, L., Amodeo, A., Augustin, P., Bach, J., Belegante, L., Biniotoglou, I.,
993 Bush, X., Comerón, A., Delbarre, H., García-Vizcaino, D., Guerrero-Rascado, J. L., Hervo, M.,

- 994 Iarlori, M., Kokkalis, P., Lange, D., Molero, F., Montoux, N., Muñoz, A., Muñoz, C., Nicolae,
995 D., Papayannis, A., Pappalardo, G., Preissler, J., Rizi, V., Rocadenbosch4, F., Sellegri, K.,
996 Wagner, F., Dulac, F., 2014b: Assimilation of lidar signals: application to aerosol forecasting
997 in the western Mediterranean basin. *J. Atmospheric Chemistry and Physics*, 14(22), 134-138.
- 998 Wiscombe, W. J., 1980: Improved MIE scattering algorithms. *J. Applied Optics*, 19(5),
999 1505-1509.
- 1000 Wu, J. B., Xu, J. M., Pagowski, M., Geng, F. H., Gu, S. Q., Zhou, G. Q., Xie, Y., Yu, Z. Q., 2015:
1001 Modeling study of a severe aerosol pollution event in December 2013 over Shanghai China: An
1002 application of chemical data assimilation. *J. Particuology*, 20(3), 41-51.
- 1003 Xia, X. L., Min, J. Z., Shen, F. F., Wang, Y. B., Yang, C., 2019: Aerosol data assimilation using data
1004 from Fengyun-3A and MODIS: application to a dust storm over East Asia in 2011. *J. Advances*
1005 *in Atmospheric Sciences*, 36, 1-14.
- 1006 Young, S. A., Vaughan, M. A. 2009: The retrieval of profiles of particulate extinction from
1007 Cloud-Aerosol Lidar Infrared Pathfinder Satellite Observations (CALIPSO) data: Algorithm
1008 description. *J. Journal of atmospheric and oceanic technology*, 26(6), 1105-1119.
- 1009 Yumimoto, K., Murakami, H., Tanaka, T. Y., Sekiyama, T. T., Ogi, A., Maki, T., 2015: Forecasting
1010 of Asian dust storm that occurred on May 10-13, 2011, using an ensemble-based data
1011 assimilation system. *J. Particuology*, 2015, 28, 121-130.
- 1012 Yumimoto, K., Nagao, T. M., Kikuchi, M., Sekiyama, T. T., Murakami, H., Tanaka, T. Y., Ogi, A.,
1013 Irie, H., Khatri, P., Okumura, H., Arai, K., Morino, I., Uchino, O., Maki, T., 2016: Aerosol
1014 data assimilation using data from Himawari-8, a next-generation geostationary meteorological
1015 satellite. *J. Geophysical Research Letters*, 43(11), 5886-5894.
- 1016 Zang, Z. Z., Li, Z. J., Pan, X. B., Hao, Z. L., You, W., 2016: Aerosol data assimilation and
1017 forecasting experiments using aircraft and surface observations during CalNex. *J. Tellus series*
1018 *B: chemical and physical meteorology*, 68(1), 1-14.
- 1019
1020
1021
1022



1023 Table 1. Numerical experiment schemes

Experiment	Assimilated data	Assimilation region	Continuous assimilation period	Forecast comparison period
Control	N/A	N/A	N/A	11.13 12:00 –11.14 12:00
DA_PM	PM _{2.5} +PM ₁₀	D01/D02	11.13 00:00 –11.13 12:00	11.13 12:00 –11.14 12:00
DA_Ext	Ext	D01/D02	11.13 00:00 –11.13 12:00	11.13 12:00 –11.14 12:00
DA_PM_Ext	PM _{2.5} +PM ₁₀ +Ext	D01/D02	11.13 00:00 –11.13 12:00	11.13 12:00 –11.14 12:00

1024

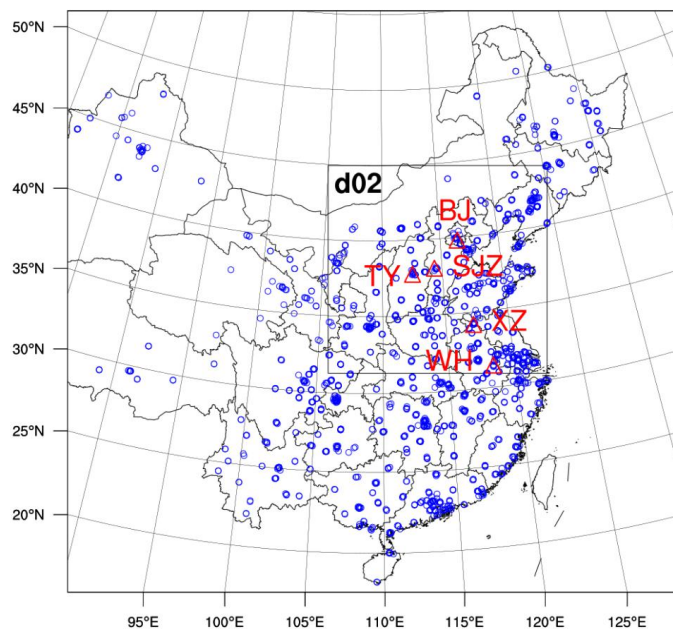
1025

1026

1027

1028

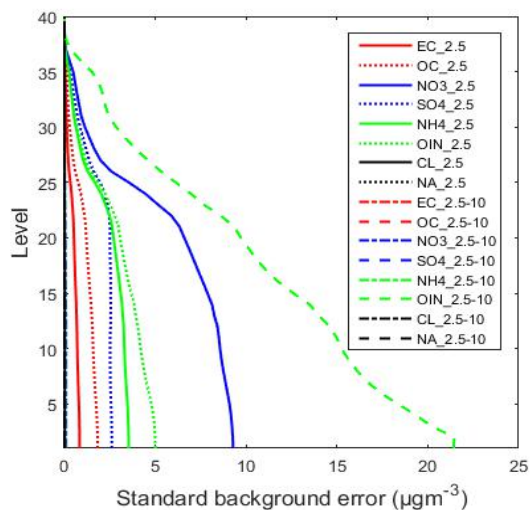
1029



1030

1031 **Figure 1** The double-nested experimental domain. Red triangle and labeling indicate the
1032 locations and names of 5 lidars, and blue circle the locations of 1500 ground environmental
1033 monitoring stations.

1034



1035

1036 **Figure 2** Vertical BESD profiles of the 16 control variables

1037

1038

1039

1040

1041

1042

1043

1044

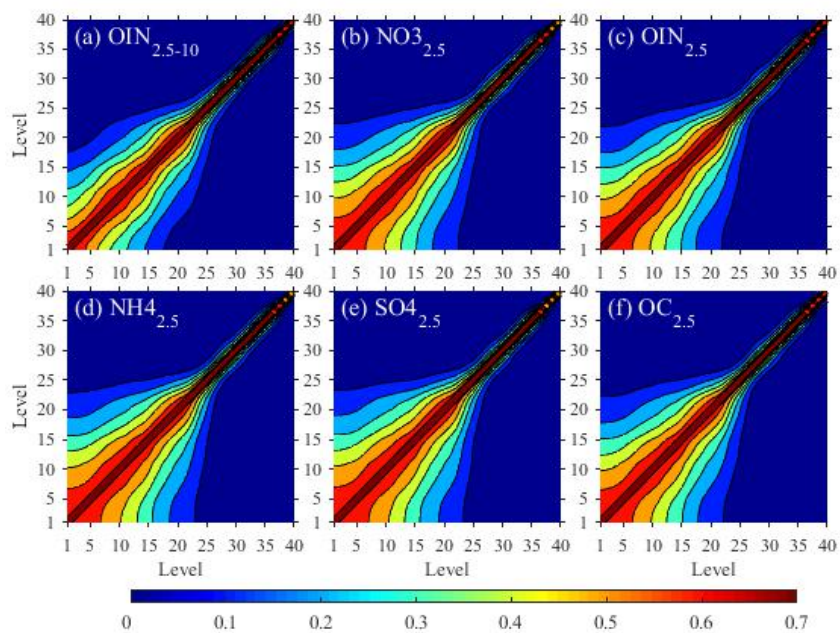
1045

1046

1047

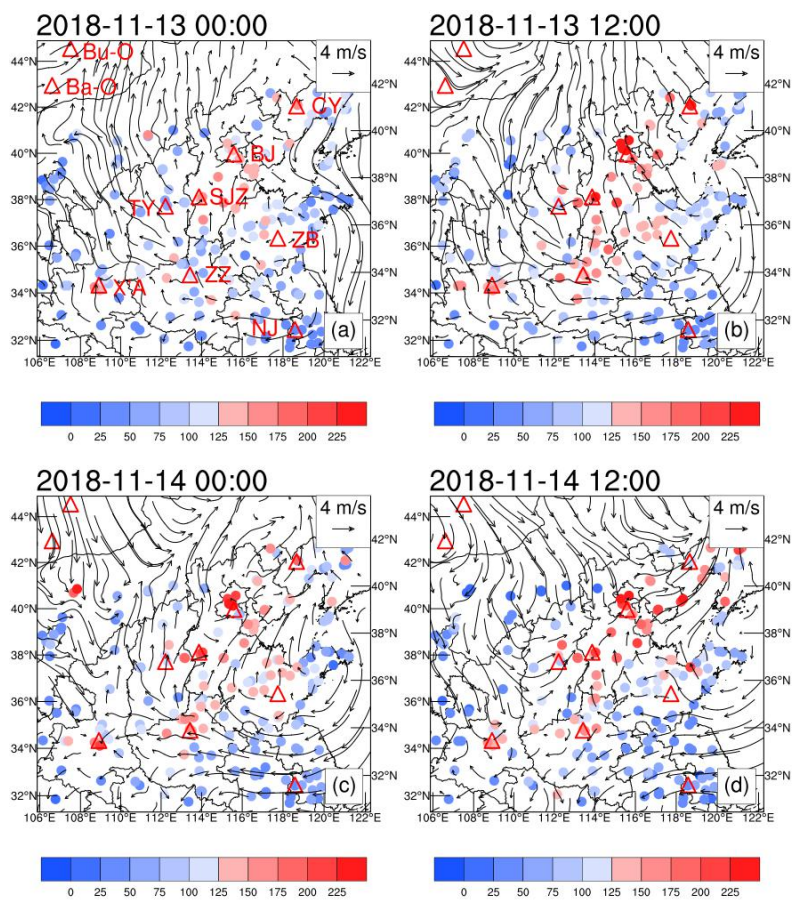
1048

1049



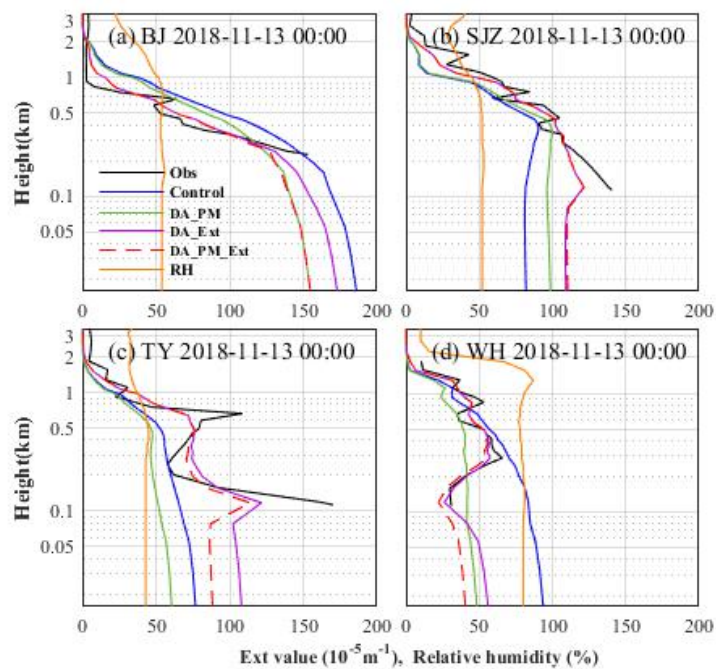
1050

1051 Figure 3 BEVCCs of six control variables



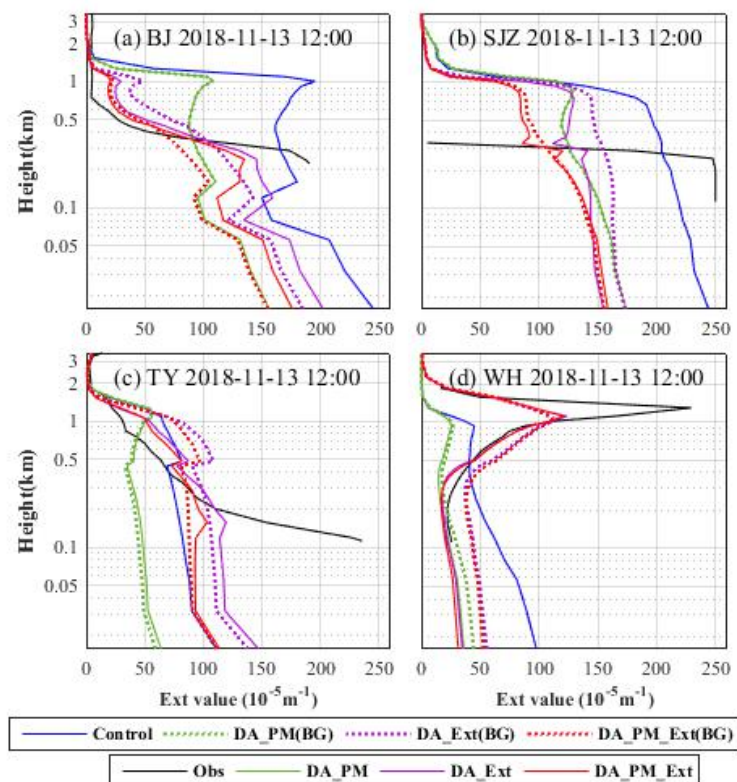
1052

1053 **Figure 4** Surface $PM_{2.5}$ MC measurements in the D02 region and NCEP reanalysis wind
1054 field for the period from 0000 UTC, November 13, 2018 to 1200 UTC, November 14, 2018
1055 (CY: Chaoyang; BJ: Beijing; SJZ: Shijiazhuang; TY: Taiyuan; ZB: Zibo; X'A: Xi'an; ZZ:
1056 Zhengzhou; NJ: Nanjing; Bu-O: Buyant-Ovoo; Ba-O: Bayan-Ovoo)



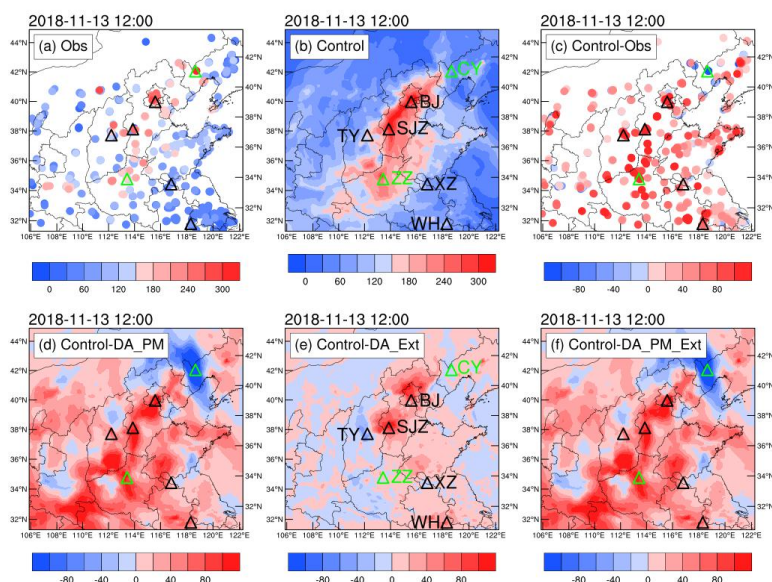
1057

1058 **Figure 5** AEC profiles at 0000 UTC, November 13, 2018 measured at four lidar stations
1059 (black lines) as well as the corresponding AEC profiles obtained from the control (blue
1060 lines) experiment and the DA_PM (green lines), DA_Ext (purple lines) and DA_PM_Ext
1061 (red lines) analysis fields and the simulated RH profiles (orange lines) (BJ: Beijing; SJZ:
1062 Shijiazhuang; TY: Taiyuan; WH: Wuhu)



1063

1064 **Figure 6** AEC profiles at 1200 UTC, November 13, 2018 measured at four lidar stations
1065 (solid black lines) as well as the corresponding AEC profiles obtained from the control
1066 experiment (solid blue lines) and the background (dotted lines) and analysis (solid lines)
1067 fields of the DA experiments (BJ: Beijing; SJZ: Shijiazhuang; TY: Taiyuan; WH: Wuhu)



1068

1069 **Figure 7** Surface $PM_{2.5}$ MCs measured at 1200 UTC, November 13, 2018 (a), as well as the
1070 initial field (b) of the control experiment and its error (c) and the distribution of differences
1071 between the initial fields of the control and DA experiments (d, e, and f) (black triangles
1072 signify the locations of the lidar stations) (BJ: Beijing; SJZ: Shijiazhuang; TY: Taiyuan; ZZ:
1073 Zhengzhou; XZ: Xuzhou; WH: Wuhu)

1074

1075

1076

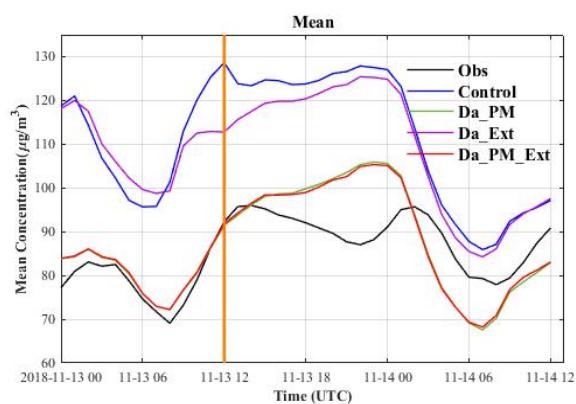
1077

1078

1079

1080

1081



1082

1083 **Figure 8** Variation in the regional mean PM_{2.5}MC with time (the vertical orange line
1084 separates the DA and forecast periods; the black line signifies measurements; the blue line
1085 signifies the PM_{2.5}MCs obtained from the control experiment; the green, purple, and red
1086 lines signify the PM_{2.5}MCs obtained from the DA_PM, DA_Ext, and DA_PM_Ext
1087 experiments, respectively)

1088

1089

1090

1091

1092

1093

1094

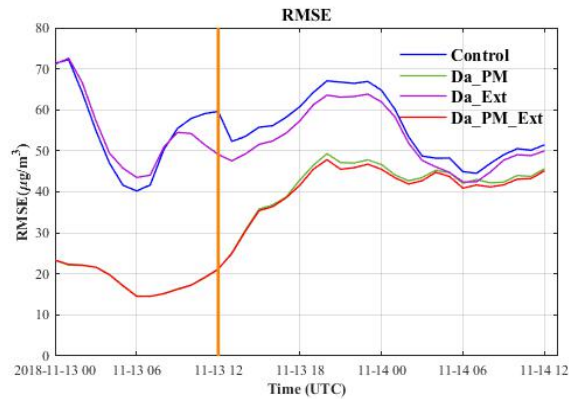
1095

1096

1097

1098

1099



1100

1101 **Figure 9** Variation in the RMSE of surface PM_{2.5}MC forecasts with time (the vertical
1102 orange line separates the DA and forecast periods; the blue line signifies the PM_{2.5}MCs
1103 obtained from the control experiment; the green, purple, and red lines signify the PM_{2.5}MCs
1104 obtained from the DA_PM, DA_Ext, and DA_PM_Ext experiments, respectively)